metals

MDPI

Article

Reduction of Residual Stresses in Cold Drawn Pearlitic Steel by a Soft Secondary Wire Diameter Reduction

Jesús Toribio * and Miguel Lorenzo

Fracture & Structural Integrity Research Group, University of Salamanca, E.P.S., Campus Viriato, Avda. Requejo 33, 49002 Zamora, Spain
* Correspondence: toribio@usal.es; Tel.: +34-677-566-723

Abstract: In this paper, the effects of the skin pass technique on the residual stress and plastic strain fields generated in cold drawn pearlitic steel wires are analyzed. The aim is to find out the optimal conditions to be used in the design of a manufacturing process for obtaining more reliable structural components in terms of the main cause of failure: the hydrogen embrittlement (HE). To achieve this goal, diverse numerical simulations were performed by using finite elements (FE) and considering, on one hand, the first step of a real cold drawing chain, using (i) a conventional drawing die and (ii) modified drawing dies with different soft diameter reductions, and, on the other hand, numerical simulations by FE of the hydrogen diffusion assisted by stress and strain states to estimate the hydrogen distributions. Obtained results revealed the secondary reduction degree as a key parameter in the die design for reducing the drawing-induced residual stress. According to the results, low values of the reduction ratio cause radial distributions of residual stress with significant reductions at both the wire core and at the wire surface. In addition, the hydrogen accumulation at the prospective damage zone (near the wire surface) given by FE simulations is lower in the wires drawn with modified drawing dies including a skin pass zone.

Keywords: prestressing steel; cold drawn pearlitic steel; wire drawing; die design; residual stress and strain; hydrogen embrittlement

check for updates

Citation: Toribio, J.; Lorenzo, M. Reduction of Residual Stresses in Cold Drawn Pearlitic Steel by a Soft Secondary Wire Diameter Reduction. *Metals* **2023**, *13*, 433. https://doi.org/10.3390/met13020433

Academic Editor: Janice Barton

Received: 1 December 2022
Revised: 3 February 2023
Accepted: 13 February 2023
Published: 20 February 2023

1. Introduction

Residual stresses generated as a result of a conforming process are a problem of the major concern in engineering. These stress states play a key role in the catastrophic failure of structural components such as prestressing steel wires that are highly susceptible to hydrogen embrittlement (HE) related phenomena [1–5]. So, any effort leading to reduce residual stress is strongly welcomed. In the particular case of the wire drawing (the conforming process widely used for obtaining commercial prestressing steel wires to be used in prestressed concrete), different methods are used in order to obtain more efficient and reliable components. On one hand, some of them are composed by diverse post-drawing treatments with the aim of releasing the stress distribution after cold drawing [6]. On the other hand, others are based on design modifications of the conforming process, mainly focused on the die geometry [7–14].

Numerical simulations by means of finite element method (FEM) are considered in many studies as a useful and reliable tool for revealing the residual stress caused after wire drawing [15–18]. Thus, FEM simulations are used for analyzing the influence of diverse parameters of the manufacturing process such as die geometry (reduction ratio, inlet die angle, bearing length, . . .) [10,14,17–22], friction [17,18,20,21], drawing speed [17,22,23], drawing steps [16], drawing force [16,19,21], back tension [16]. In addition, FEM simulations were also used for studying the benefits of innovative designs of wire drawing process [14,23,24]. Furthermore, FEM simulations are applied for the analysis of the role of material behavior analyzing the material strain hardening [17,25,26]. Moreover, FEM simulations are widely used for the analysis of the generation and evolution of defects during wire drawing [27–29] and their influence on fracture-related phenomena [30,31]. In addition, the influence of inclusions on fracture of cold drawn wires are analyzed in multiple studies by means of FEM simulations [32,33].

It is worth to point out that an improvement of the mechanical behaviour against fatigue is achieved when residual stresses of compressive nature are generated near the wire surface [34]. Thus, today, the use of surface post-treatments such as shot peening (whose aim is to introduce a compressive stress in the vicinity of the component surface) is widespread in industry for increasing the life of parts undergoing fatigue loading. Taking into account the same idea, to promote a compressive stress state at the part surface, a process known as skin pass is also used [12,13]. Briefly, this one consists of applying a soft reduction of the wire diameter at the end of the drawing chain. In certain cases, the skin pass is performed in the same drawing die [12]. According to [12], a final reduction of 1–5% of the wire diameter, developed in the same die, causes a significant reduction and redistribution of the stress state.

Cold drawn wires are highly susceptible to hydrogen-damage-related phenomena, in particular to HE [35,36]. Stress and strain state plays a key role in the main stage of such a phenomenon: the hydrogen diffusion from the hydrogenation surface towards prospective damage zones. The variables representing the stress and strain state in the well-known hydrogen diffusion model [37–42] are the inwards gradient of hydrostatic stress and the inwards gradient of hydrogen solubility dependent on equivalent plastic strain. These variables act as driving forces for hydrogen diffusion and, hence, hydrogen is diffused from the hydrogenation surface towards inner points with (i) lower hydrogen concentration, (ii) higher hydrostatic stress and (iii) higher hydrogen solubility that depends on equivalent plastic strain.

Unfortunately, there is a lack of information with regard to the influence of skin pass on the stress redistribution of the aforesaid variables and, therefore, on hydrogen diffusion causing HE in prestressing steel wires. So, to fill this gap, in this paper, the effects of the skin pass on the reduction and redistribution of the manufacturing-induced residual stress and strain fields in cold drawn pearlitic steel wires are analyzed. Special attention is paid to the variables involved in the hydrogen diffusion assisted by stress and strain causing HE: the hydrostatic stress and the equivalent plastic strain. To achieve this goal, diverse wire drawing processes were simulated by means of finite elements considering modified drawing dies with different soft secondary reductions degrees, to reveal the residual stress and strain states. The obtained results are compared with the residual stress and strain fields obtained after the first step of an industrial wire drawing process with conventional dies, i.e., without skin pass zone, used for obtaining a real commercial prestressing steel wire. In addition, a numerical simulation by FE of the hydrogen diffusion assisted by stress and strains were carried out in order to estimate the hydrogen accumulation in wires drawn using a conventional die and using an optimal skin pass die (including a soft secondary wire diameter reduction) from the mechanical point of view. This way, the improvement of the mechanical behaviour of the wires in inert and hydrogenating environments can be estimated, and the optimal values for developing the modified wire drawing are revealed.

2. Materials and Methods

The numerical simulation of wire drawing was carried out considering diverse die geometries by means of a commercial FEM code (MSC.Marc). The geometry of a conventional die (Figure 1a) can be divided into two main zones: the wire reduction zone (A–B in Figure 1a) and the bearing length zone (B–C in Figure 1a). According to the study [10], soft variations of the inlet die angle (α) produce significant variations on the plastic strain and the residual stress distributions, whereas such changes on the residual stress and strain state are only noticeable when the bearing length (l_z) is lower than a characteristic value ($l_z = d_0$), d_0 being the initial wire diameter. However, for defining the geometry of the modified drawing die where a secondary soft reduction (CD zone in Figure 1b) after the main bearing length (BC zone in Figure 1b), two additional parameters are needed: the secondary die angle (α_2) and the secondary diameter reduction (Δd_2).

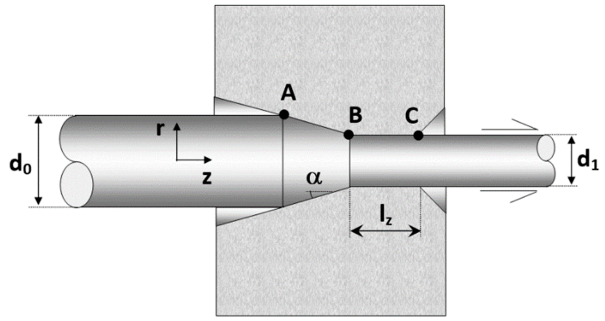

(**a**)

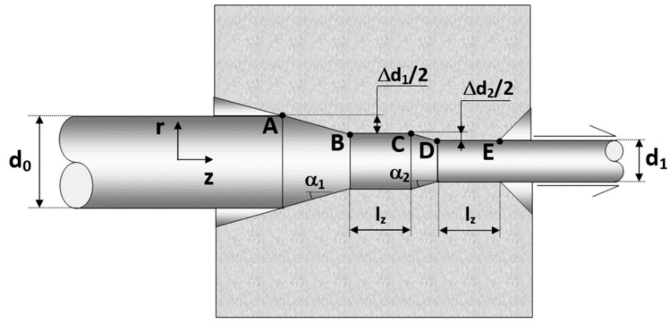

(**b**)

Figure 1. Scheme of (**a**) conventional wire drawing die and (**b**) a wire drawing die including a skin pass zone after the bearing length of the main reduction.

To reveal the influence of the secondary reduction (Δd_2 in Figure 1b) on the residual stress and strain states after wire drawing with modified drawing dies, four different numerical simulations of the first step of a commercial wire drawing process were carried out. In this drawing step, the cross-sectional area of the wire is reduced from an initial diameter d_0 = 12.0 mm to a final one d_1 = 10.8 mm (wire radius, a = 5.4 mm). For the modified drawing dies including the skin pass zone, the whole drawing step diameter reduction (Δd = 1.2 mm) is divided into two consecutive reductions: the main reduction (Δd_1 in Figure 1b) and the secondary reduction (Δd_2 in Figure 1b).

A dimensionless parameter called *skin pass reduction ratio* λ, defined as $\lambda = \Delta d_2/\Delta d$, is used in this study. This way, the following reduction ratios were considered in the analysis: (i) a slight reduction $\lambda = 1/24$, i.e., Δd_1 = 1.15 mm and Δd_2 = 50 µm, two medium reductions, (ii) $\lambda = 1/12$, i.e., Δd_1 = 1.10 mm and Δd_2 = 100 µm, (iii) $\lambda = 1/6$, i.e., Δd_1 = 1.00 mm and Δd_2 = 200 µm, and finally (iv) a high reduction $\lambda = 1/3$, i.e., Δd_1 = 0.80 mm and Δd_2 = 400 µm. For all the cases, the same bearing length ($l_z = d_0$) was considered after the main and secondary reductions.

Finally, an inlet die angle commonly used in conventional wire drawing was chosen for both the primary and the secondary reductions ($\alpha_1 = 7°$, $\alpha_2 = 7°$). Axisymmetric formulation was applied due to the radial symmetry of both wire and die considering elastoplastic large deformations with updated Lagrangian formulation. Several meshes were used until required mesh convergence was achieved. The material considered in simulations is a pearlitic steel obtained from a real drawing chain with the following chemical composition: 0.800% C, 0.690% Mn, 0.230% Si, 0.012% P, 0.009% S, 0.004% Al, 0.265% Cr, 0.060% V [43]. The pearlite colony of the hot rolled bar analyzed in this study can be considered as an ellipsoidal geometry according to [44]. Thus, the longitudinal section and transverse section of such ellipsoid are ellipses with the following axis length: 20 µm and 10 µm at the longitudinal section; 15.2 µm and 14.8 µm at the transversal section according to the analysis developed in the study [44]. The interlamellar spacing of the hot roller bar is 0.056 μm according to [45].

In this paper, the same steel was used in all the numerical simulations. The constitutive model applied was elastoplastic solid with von Mises yield surface, associated flow rule, and isotropic strain-hardening according to [43]. Conventional tension tests up to fracture (Figure 2a) were carried out under a constant displacement rate of 2 mm/min in a universal test machine (MTS RF/200), in order to reveal the mechanical properties of the pearlitic steel used in FEM simulations. Samples of 300 mm length of hot rolled bars corresponding to a real commercial wire drawing chain were tested. From the test results, the material true stress and true strain curve was revealed (Figure 2b) allowing to obtain the following mechanical properties: Young modulus, E = 194 GPa and yield strength, σ_Y = 720 MPa.

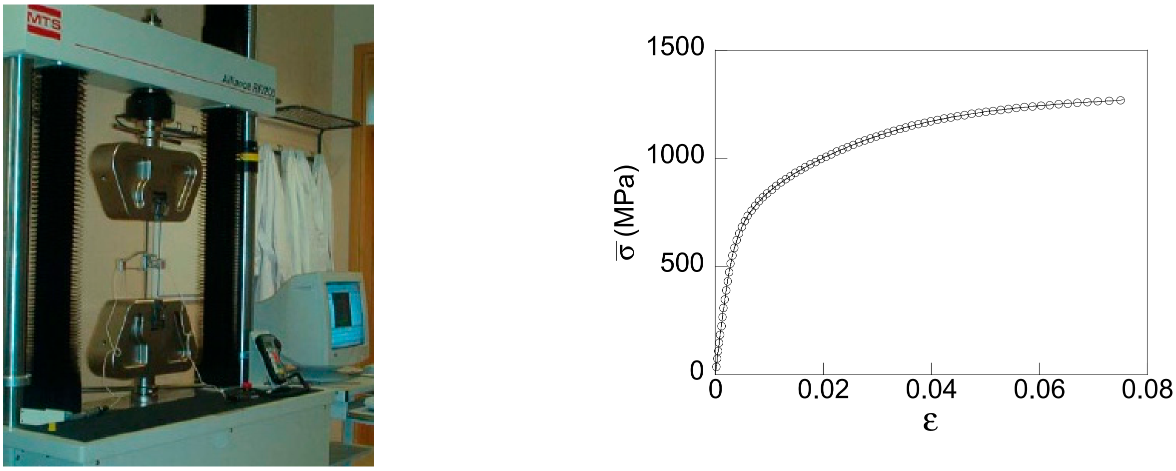

(**a**) (**b**)

Figure 2. Conventional tension test: (**a**) experimental set-up and (**b**) experimental stress–strain curve of the raw material before cold drawing.

Commonly, conventional drawing dies are made with ceramic materials such as tungsten carbides since a high stiffness, strength and resistance to wear are essential requirements for obtaining a wire with the specified dimensions at the end of wire drawing. Thus, in this study, dies were modeled as rigid bodies since this one can be considered as a fine approach to the real behaviour of such a component during drawing. Wire was modelled as a deformable body with a non-uniform mesh of 4-nodes quadrilateral elements. Thus, the element size is progressively increased from the wire center up to the wire-die contact zone where a fine mesh is required. A mesh convergence test was carried out in order to select the most adequate mesh for calculations. As results, a mesh of 3381 nodes and 3200 elements was considered in FEM simulations.

With regard to the boundary conditions, nodes placed at the wire symmetry axis were fixed in the radial direction due to the axisymmetric geometry. In addition, a linearly increasing displacement was imposed at the nodes located at the front extreme of the wire up to reaching a final displacement that places the wire completely out of the die. The slope of this linear variable displacement is related to the drawing speed; thus, a commonly used drawing speed of 50 mm/s was included in the simulations. Previous studies revealed that friction does not influence on final stress distributions after wire drawing [27] and, for this reason, this parameter was not included in the FEM simulations, selecting a frictionless contact between the die and the wire.

3. Stress and Strains Induced by Cold Drawing

FEM simulations reveal the stress and strain fields during and after the first drawing step. The chromatic maps (Figures 3 and 4) qualitatively show the main changes in axial and hydrostatic stress fields when modified dies (including a skin pass zone) are used, compared to the those generated with conventional dies. To go further in the analysis, the radial distribution, from the wire center at the wire symmetry axis $r = 0$ to the wire surface $r = 5.6$ mm, of axial stress and hydrostatic stress obtained for wires drawn with different secondary reduction degrees are shown in Figure 5a and Figure 5b, respectively, compared with those obtained after a conventional process (filled circles).

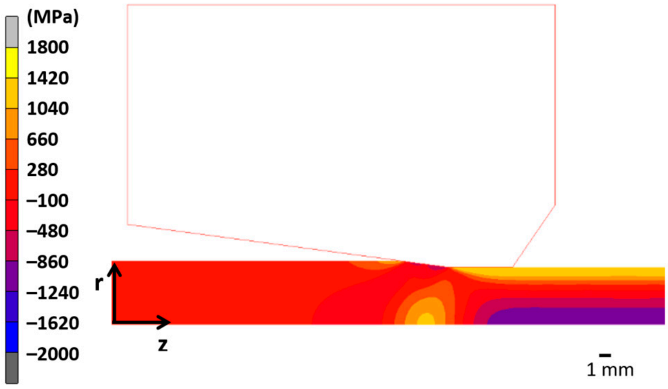

(**a**)

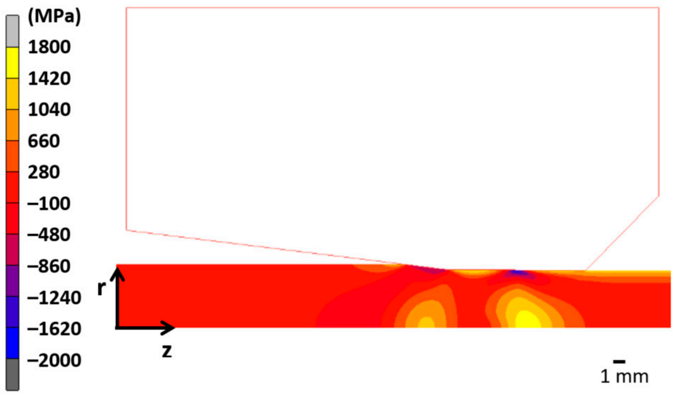

(**b**)

Figure 3. Axial stress fields obtained in: (**a**) a conventional cold drawing process and (**b**) a cold drawing with modified dies including a skin pass zone.

The main differences may be summarized as follows: (i) the axial and the hydrostatic stress after drawing with modified dies are significantly reduced at the inner points of the wire and (ii) reductions in the vicinity of the wire surface are also obtained.

Figure 5a,b reveals the secondary reduction (Δd_2) as a key parameter in the redistribution of residual stress after cold drawing with modified dies including a skin pass soft reduction. Thus, for high secondary reduction ($\lambda = 1/3$), the shape of both axial and hydrostatic stress distributions are similar to that obtained in a conventional process. This way, in the axial stress distribution shown in Figure 5a, a tensile stress zone appears close to the wire surface (3.8 mm $< r <$ 5.4 mm) and lowers with depth ($x = d/2 - r$) up to becoming of compressive nature for $r <$ 3.8 mm with the same decreasing trend up to the wire core. Nevertheless, the stress distribution is deeply changed for low values of the reduction ratio λ. Thus, the tensile stress zone is narrower (4.2 mm $< r <$ 5.4 mm) and compressive stresses are distributed almost uniformly at the inner points. In the case of the lowest reduction ratio ($\lambda = 1/24$), a compressive zone appears placed close to the wire surface (3.8 mm $< r <$ 5.1 mm). As results, a tensile zone is found at the half of the wire radius (0.8 mm $< r <$ 3.8 mm) with a slight compressive zone near the wire center.

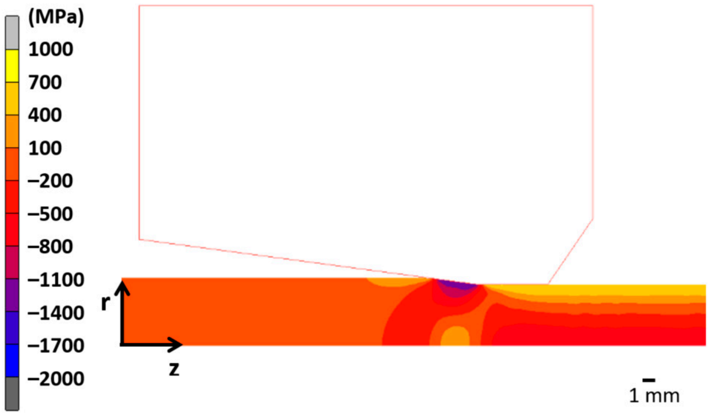

(**a**)

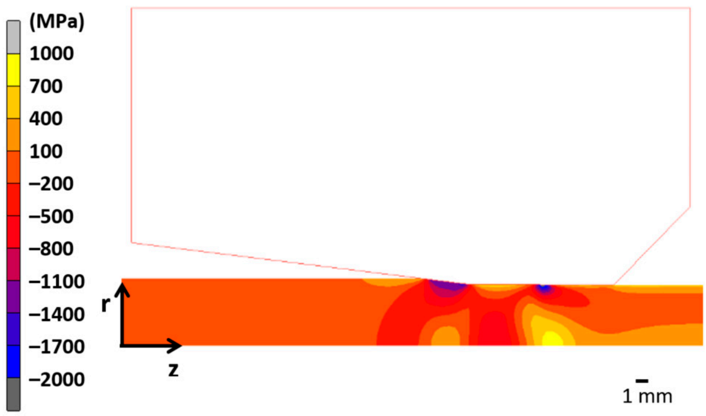

(**b**)

Figure 4. Hydrostatic stress fields obtained in: (**a**) a conventional cold drawing process and (**b**) a cold drawing with modified dies including a skin pass zone.

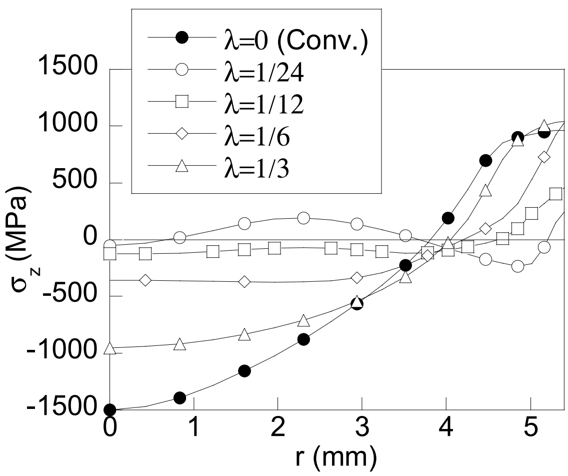

(**a**)

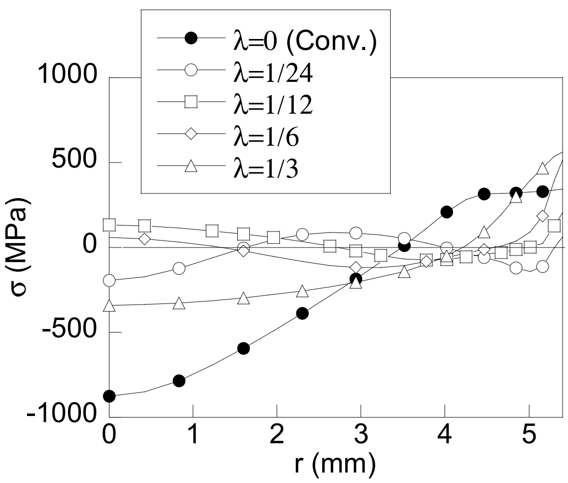

(**b**)

Figure 5. Radial distribution of the residual (**a**) axial stress and (**b**) hydrostatic stress, in cold drawn wires using diverse values of the secondary reduction ratio.

With regard to the hydrostatic stress distributions (Figure 5b), a similar effect is observed but, in this case, the initial compressive stress zone ($0 < r < 3.5$ mm) becomes slightly tensile at the wire core surroundings ($0 < r < 2.0$ mm) for reduction ratios $\lambda = 1/12$

and $\lambda = 1/6$. As in the case of axial stress, the distribution of the hydrostatic stress obtained for the lowest reduction ratio ($\lambda = 1/24$) exhibits a zone of compressive stress near the wire surface (4.0 mm < r < 5.2 mm) and a tensile stress zone in the middle of the wire radius (2.0 mm < r < 4.0 mm) becoming compressive at the wire center.

From obtained results, two interesting effects can be highlighted. On one hand, as the parameter Δd_2 decreases, the axial stress state of compressive nature at the wire core decreases up to a 90% of the axial stress corresponding to a conventional cold drawn wire. A similar reduction is obtained in the hydrostatic stress distribution but, in this case, the stress state is of tensile nature. On the other hand, the axial stress at the wire surface is progressively reduced with the parameter λ, reaching a reduction of 50% for $\lambda = 1/12$ and a 75% for the lowest one ($\lambda = 1/24$). In the case of the hydrostatic stress at the wire surface (σ_Γ), results show an increment of this variable (60%) for high reduction ratios ($\lambda = 1/3$) with regard to the conventional wire drawing. Nevertheless, the value of σ_Γ decreases with the reduction ratio λ, and this way, a final reduction of 40% of the hydrostatic stress at the wire surface is obtained with a modified die considering a reduction ratio of $\lambda = 1/12$, whereas the reduction is about 80% for the lowest reduction ratio $\lambda = 1/24$. So, these cases (reduction ratios of $\lambda = 1/12$ and $\lambda = 1/24$) seem to be optimal for obtaining cold drawn wires with lower residual stress than conventional cold drawn wires since high reductions of both axial and hydrostatic stress state are obtained, resulting in a more uniform radial distribution of these variables.

In a similar way, Figure 6 shows the equivalent plastic strain field during wire drawing and Figure 7 shows the radial distribution of equivalent plastic strain, from the wire center at the wire symmetry axis $r = 0$ to the wire surface $r = 5.6$ mm, obtained in the wire drawn with diverse secondary reduction degrees compared with the one obtained in a conventional cold drawing (filled circles).

According to the obtained results, the wire drawn using modified dies exhibits a less homogenous distribution of plastic strain, reaching higher values than those produced in a conventional drawing process. This effect is particularly relevant at the wire surface surroundings (3 mm< r <5.4 mm). For deeper points, such an increment progressively vanishes with depth from the wire surface up to disappearing nearby the wire core (r < 2 mm) where similar plastic strain is obtained for all analyzed cases. According to these results, the maximum equivalent plastic strain generated in the wire after cold drawing increases with the reduction ratio λ, except for the highest value considered of such a parameter ($\lambda = 1/3$).

As can be noticed in Figure 7, the highest increment of the maximum equivalent plastic strain (obtained for $\lambda = 1/6$) is around 50% higher than the one obtained with a conventional drawing whereas for the other cases of study is around 35% ($\lambda = 1/12$) and 20% ($\lambda = 1/24$) respectively. In addition, Figure 7 reveals that the position where the maximum equivalent plastic strain appears is also affected by the reduction ratio λ. Thus, for low secondary reductions ($\lambda = 1/12$ and $\lambda = 1/24$) the maximum is placed at the wire surface and, as this parameter is increased, the position of such a maximum is moved towards inner points of the wire.

Thus, a positive inwards gradient of equivalent plastic strain is obtained for high values of λ whereas low reduction ratios exhibit a negative inwards gradient. In addition, for higher reduction ratios, a wider high strained zone is obtained. It is also interesting to analyze changes in the equivalent plastic strains at the wire surface. There, an increment of 25% of equivalent plastic strain is obtained for the highest reduction ratio ($\lambda = 1/3$) whereas the increment is about 40% for the secondary reduction ratio $\lambda = 1/12$. The lowest increment, about 20% is obtained for the lowest reduction ratio ($\lambda = 1/24$).

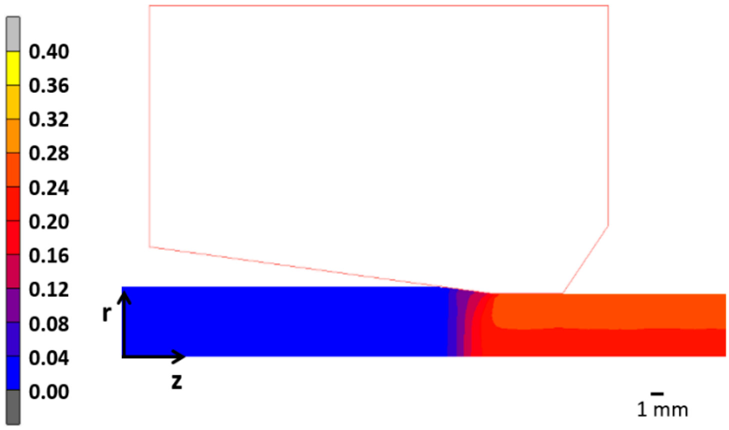

(**a**)

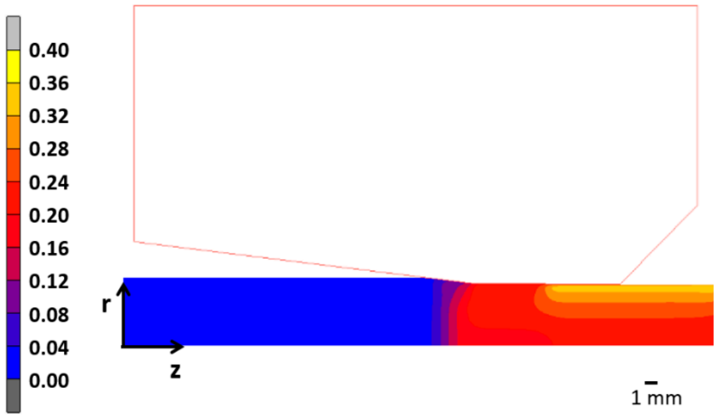

(**b**)

Figure 6. Equivalent plastic strains fields obtained in: (**a**) a conventional cold drawing process and (**b**) a cold drawing with modified dies including a skin pass zone.

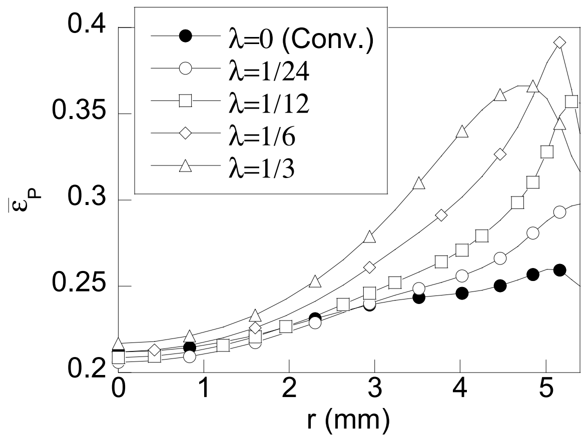

Figure 7. Radial distributions of equivalent plastic strain in cold drawn wires using diverse values of the secondary reduction ratio.

Following the previous analyses, the optimum conditions for the wire drawing are obtained using low values of the secondary reduction since, under such conditions, not only a substantial reduction of residual stresses (both axial and hydrostatic) is obtained at the wire core but also at the wire surface. For achieving a better approach for the optimal case of the skin pass technique applied to prestressing steel wires, additional cases corresponding to different values of the secondary reduction were considered as follows: Δd_2 = 20 μm (λ = 1/60), Δd_2 = 75 μm (λ = 1/16) and Δd_2 = 150 μm (λ = 1/8).

The optimal case from the structural integrity point of view can be considered as that reducing residual stresses and generating more uniform stress distributions. So, to find out such a case, the values of the key features of the stress distribution for axial and hydrostatic stress, namely: (i) the stress at the wire surface, σ_Γ, (ii) the stress at the wire core, σ_0, and finally (iii) a measure of the uniformity of the stress distribution: the average stress, σ_m, are represented in Figure 8a,b, for all the cases of the study. In a similar way, Figure 9 shows two key parameters of the distribution of equivalent plastic strain, namely: (i) the maximum value of the equivalent plastic strain and (ii) the value of such a variable at the wire surface.

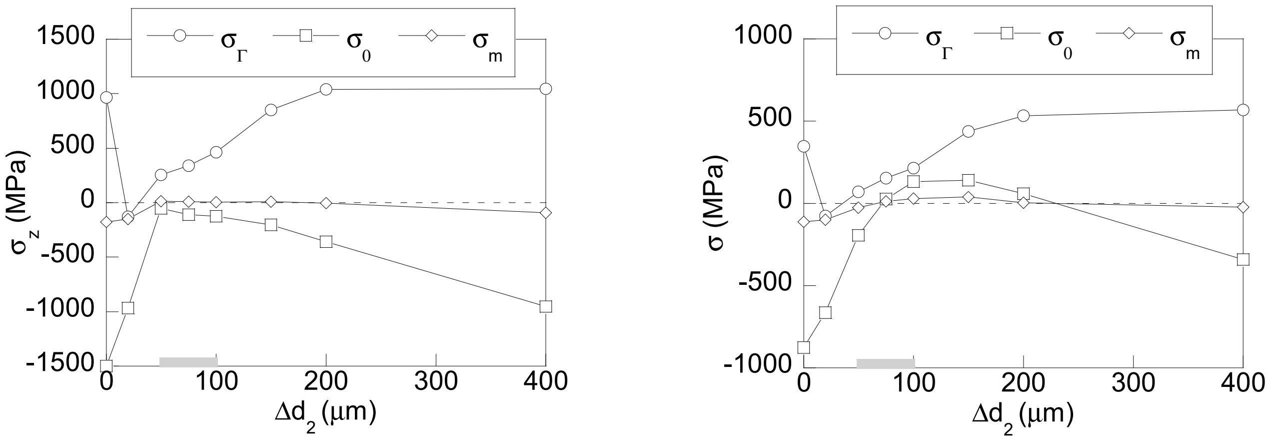

(**a**) (**b**)

Figure 8. Variation of stress at the wire surface, the wire core and average stress with the secondary reduction applied in a skin pass wire drawing die for: (**a**) axial stress and (**b**) hydrostatic stress.

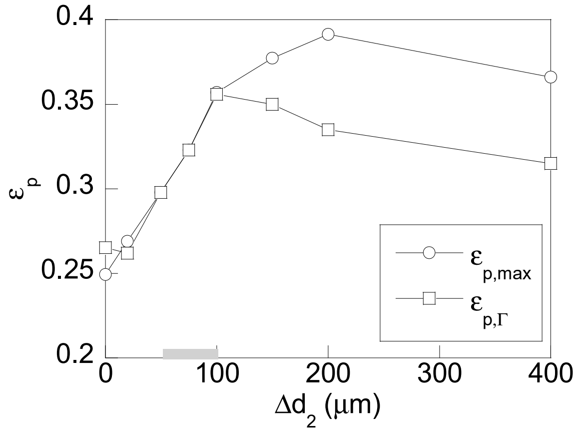

Figure 9. Variation of equivalent plastic strain at the wire surface, and maximum plastic strain with the secondary reduction applied in a skin pass wire drawing die.

According to results plotted in Figure 8, a progressive reduction of both axial and hydrostatic stress at the wire core and of average stress is achieved as the secondary reduction is increased from conventional wire drawing (λ = 0) up to the case corresponding to λ = 1/24 (Δd_2 = 50 μm) where the minimum axial stress at wire core (almost null) is reached. Hereafter, the trend changes for higher values of the secondary reduction and the axial stress at the wire core is progressively increasing with the reduction ratio λ, it always being of compressive nature.

In the case of hydrostatic stress at the wire core (Figure 8b), tensile stress appears for secondary reduction within the range 75 µm < Δd_2 < 200 µm. For higher values of Δd_2, the stress state returns to be of compressive nature, increasing the value of hydrostatic stress with the secondary reduction. According to the variation shown in Figure 8b, the stress reduction at the wire surface is progressively lower as the secondary reduction is increased. Thus, the maximum reduction of the stress state at the wire surface is obtained for the lowest reduction ratio considered, $\lambda = 1/60$ (Δd_2 = 20 µm). Notice that, for values of Δd_2 higher than 100 µm, the stress at the wire surface overcome that obtained by using conventional dies.

Thus, the optimal case from the mechanical point of view for reducing the residual stress state is within the range of values between Δd_2 = 50 µm and Δd_2 = 100 µm (shaded line in Figure 8), since within such a zone, the lowest values of the stress at the wire surface and at the wire core are obtained without significantly increasing the average stress. Unfortunately, the maximum reductions at the wire surface and at the wire core are not reached for the same value of secondary reduction. So, the optimum case depends on if the maximum stress reduction has to be located at the wire core or at the wire surface.

With regard to the equivalent plastic strain (Figure 9), the maximum plastic strain and the plastic strain at the wire surface are similar for low values of the secondary reduction up to Δd_2= 100 µm (λ = 1/12). For these cases, the equivalent plastic strain increases with the value of Δd_2 and for high secondary reductions, the equivalent plastic strain at the wire surface is progressively reduced. However, the maximum plastic strain is still increased up to a reduction ratio of λ = 1/6 (Δd_2 = 200 µm), and later it decreases for higher reduction ratios. Within the optimal zone according to stress reductions analyzed in Figure 8, $\Delta d_2 \in$ (50 µm, 100 µm), the increment of plastic strains is within the range 20–40% compared to the values obtained for a conventional drawing. According to these results, the maximum value of the equivalent plastic strain is always reached at the wire surface for values included within the optimal range. This fact means that the inwards gradient of equivalent plastic strains is negative and, consequently, it acts against hydrogen diffusion towards the inner points of the wire.

4. Hydrogen Embrittlement

To achieve a better understanding of the implications on the HE of previously discussed changes in the stress and plastic strain distributions, a brief description of the governing equations of the main stage of HE, the hydrogen diffusion within the metal lattice, seems to be adequate [37–42]. Hydrogen diffuses from the wire surface to inner points as a function of the inwards gradients of both hydrostatic stress (σ) and hydrogen solubility ($K_{s\varepsilon}$) as follows [37–42]:

$$\boldsymbol{J} = -D(\bar{\varepsilon}_{\mathrm{P}})\left\{\nabla C - C\left[\frac{V_{\mathrm{H}}}{RT}\nabla\sigma + \frac{\nabla K_{\mathrm{S}\varepsilon}(\bar{\varepsilon}_{\mathrm{P}})}{K_{\mathrm{S}\varepsilon}(\bar{\varepsilon}_{\mathrm{P}})}\right]\right\}, \tag{1}$$

$\boldsymbol{J}$ being the hydrogen flux, D the diffusion constant, C the hydrogen concentration, R the molar gas constant, V_{H} the partial volume of hydrogen, T the absolute temperature and $K_{s\varepsilon}$ the hydrogen solubility that is a function of equivalent plastic strain [39].

The hydrogen diffusion equation can be expressed as a second-order partial differential equation applying the matter conservation law and the Gauss–Ostrogradsky theorem, thereby resulting:

$$\frac{\partial C}{\partial t} = \nabla \cdot \left[D\nabla C - DC\left(\frac{V_{\mathrm{H}}}{RT}\nabla\sigma + \frac{\nabla K_{\mathrm{S}\varepsilon}(\bar{\varepsilon}_{\mathrm{P}})}{K_{\mathrm{S}\varepsilon}(\bar{\varepsilon}_{\mathrm{P}})}\right)\right]. \tag{2}$$

The steady-state solution of previous equation represents the equilibrium concentration of hydrogen for infinite time of exposure to hydrogenating environment (C_{eq}) in the form of a Maxwell–Boltzman type distribution as follows:

$$C_{eq} = C_0 K_{S\varepsilon}(\bar{\varepsilon}_P) \exp\left[\frac{V_H}{RT}\nabla\sigma\right], \tag{3}$$

where C_0 is the equilibrium hydrogen concentration for the material free of both stress and strain fields.

Therefore, hydrogen diffuses toward inner points due to: (i) the negative gradient of hydrogen concentration; (ii) the positive gradient of hydrostatic stress; (iii) the positive gradient of hydrogen solubility, which is related to the gradient of equivalent plastic strain ($K_{s\varepsilon} = 1 + 4\varepsilon_P$ [39]). This way, the analysis of the plastic strain gradient will lead to similar results to those obtained analyzing hydrogen solubility gradient considering the linear dependence of the latter variable on equivalent plastic strain.

A FEM simulation of the hydrogen diffusion assisted by stress and strains was carried out in order to reveal the hydrogen accumulation in wires drawn with both conventional dies and the optimal die (*non-conventional*) from the mechanical point of view, as previously discussed. Similar hydrostatic stress and equivalent plastic strains fields are obtained after cold drawing by FEM in the wire radial direction (cf. Figures 4 and 6). Consequently, variations on the axial direction are negligible and a one-dimensional (1D) axisymmetric approach can be used for the analysis of hydrogen diffusion assisted by stress and strains to reveal the hydrogen accumulation on the wire. This way, a FEM numerical simulation of the axisymmetric boundary-value problem of stress-strain affected diffusion (Equation (2)) was implemented in a general propose mathematical software. The Galerkin method was applied considering the same element shape functions $N_e(r)$ as trial and weighting functions in usual terms [39]. In addition, the hydrostatic stress $\sigma(r)$ and equivalent plastic strain $\varepsilon_P(r)$ radial distributions were approximated using the same shape functions as follows:

$$\sigma(r) = \sum \sigma_j N_j(r), \varepsilon_P(r) = \sum \varepsilon_{Pj} N_j(r), \tag{4}$$

where $j = 1, \ldots, M$ corresponds to the number of node of the FEM mesh, M being the total number of nodes.

The weak form of the weighted residual statement of the problem rendered the system of ordinary differential equations with respect to the FEM nodal concentration values $C_j(t)$ as the functions of time as follows:

$$[M_{ij}]\left\{\frac{dC_j}{dt}\right\} + [K_{ij}]\{C_j\} = \{F_i\} \ (i, j = 1, \ldots, M), \tag{5}$$

where the components of the element matrices [...] and the vector-columns {...} are, respectively:

$$M_{ij} = \int_V N_i N_j dV, \tag{6}$$

$$K_{ij} = \int D(\varepsilon_P)\left\{\nabla N_i \nabla N_j - \left[\left(\frac{V_H}{RT}\nabla\sigma + \frac{\nabla K_{S\varepsilon}(\varepsilon_P)}{K_{S\varepsilon}(\varepsilon_P)}\right)\cdot\nabla N_i\right] N_j\right\} dV, \tag{7}$$

$$F_i = -J_s \int_{S_f} N_i dS, \tag{8}$$

applying the flux of hydrogen J_S on the part S_f of the surface, whenever convenient.

Finally, the first-order differential Equation (5) can be solved by programming the time-marching numerical scheme proposed for diffusion-type equations [46]. This way, for the *m-th* time interval [t_{m-1},t_m], the nodal concentration values C_{m-1} and C_m are obtained from the following equation:

$$(C_m - C_{m-1})(\mathbf{M} + \theta\ \Delta t\ \mathbf{K})/\Delta t + \mathbf{K}C_{m-1} = \mathbf{F} \quad (9)$$

where $\Delta t = t_m - t_{m-1}$, and θ must assure the stability of this time-marching scheme. The imposed initial conditions C_0 are included in the first time interval (at m = 1). Afterwards, the solution of the following matrix equation gives the values for hydrogen concentration of the following time interval C_m:

$$C_m = C_{m-1} + (\mathbf{M} + \theta\ \Delta t\ \mathbf{K})^{-1}(\mathbf{F} - \mathbf{K}C_{m-1})\Delta t \quad (10)$$

Thus, the hydrogen distribution for any time during exposure to the hydrogenating environment can be obtained. The described procedure of time integration was proven to be unconditionally stable when the parameter θ is between 0.5 and 1, i.e., θ ∈ [0.5, 1].

For the sake of simplicity, the same mesh discretization used in the numerical modelling of the wire drawing was considered for simulating the hydrogen diffusion assisted by stress and strain, assuming linear trial functions for both space and time variables. The parameters involved in the simulations were chosen as follows: fixed temperature, T = 298 K; partial molar volume of hydrogen for iron-based alloys, V_H = 2 cm^3/mol [47]. In this study, the hydrogen diffusivity D for the hot rolled bar A0 was taken from previous studies as follows: $D = 6.6 \times 10^{-11}$ m^2/s [48].

From numerical simulations, the radial distributions of hydrogen concentrations, from the wire center at the wire symmetry axis r = 0 to the wire surface r = 5.6 mm, were estimated (Figure 10) for both a conventionally drawn wire and for wires drawn with *non-conventional* (*innovative*) modified dies for short times of exposure to hydrogen environment (24 h) and for long times of exposure (200 h). For the sake of clarity, only three cases are represented in Figure 10: (i) the conventional wire drawing and (ii) wires drawn with the optimal reduction ratios according to the previously discussed, (λ = 1/12 and λ = 1/24).

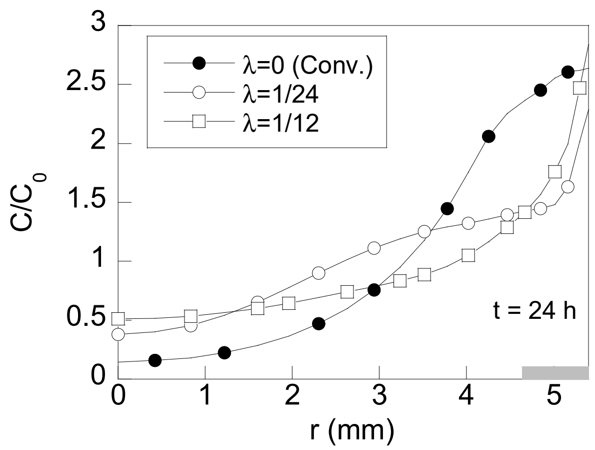

(**a**)

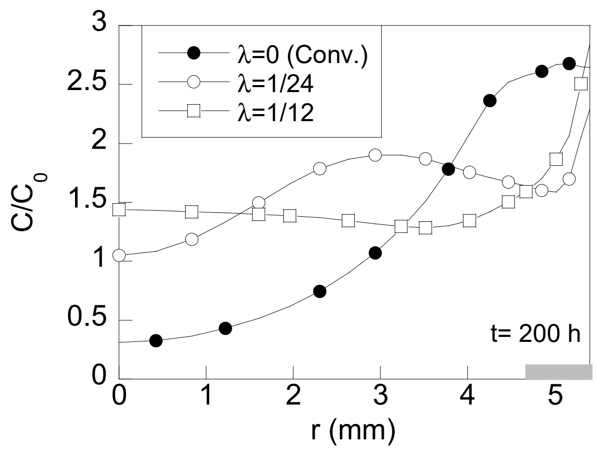

(**b**)

Figure 10. Radial distribution of hydrogen concentrations in cold drawn wires using conventional dies (filled circles) and *non-conventional (innovative*) modified dies including a skin pass zone with optimal secondary reduction ratios (blank symbols): (**a**) after 24 h and (**b**) after 200 h of exposure to a hydrogenating environment.

The radial distribution of hydrogen concentration reveals that changes in stress and plastic strains caused by a wire drawing including dies with skin pass zones are beneficial from the HE point of view. Thus, a significant reduction of the hydrogen content as high as 40% for λ = 1/24 and 30% for λ = 1/12 is obtained for short (24 h) and long times (200 h) of exposure to a hydrogenating environment at the wire surface surroundings. Notice that, according to [49–53], such a zone is the place where the prospective damage zone (x = 450 µm, r/a = 0.90) appears in these wires. However, for inner points of the wire (0 < r < 3.5 mm), a higher hydrogenation than the one obtained using conventional dies is reached at the wire core. This effect is due to the reduction of the negative hydrostatic stress (Figure 5b) cancelling the beneficial effect of compressive stresses on hydrogen accumulation observed in a conventional wire drawn. For long times of exposure, the hydrogen concentration at the inner points of the wire is significantly increased (see Figure 10b), but it is worth to point out that the hydrogen amount is always lower (about a 75% for the reduction ratio 1/12 and 30% for the reduction ratio 1/24) than the one obtained in conventional wires at the prospective damage zone.

In addition, the hydrogen concentration at the wire surface is an indicator of the hydrogen potentially diffusible towards the inner points of the wire. Two competitive effects influence on this variable in wires drawn with modified dies: on one hand, the increment of equivalent plastic strains and, on the other hand, the reduction of hydrostatic stress. Thus, the analysis of such a parameter reveals that a slight increment of 10% is obtained for a wire drawn using dies with a reduction ratio of $\lambda = 1/12$, whereas a reduction of 10% is reached for dies with a reduction ratio of $\lambda = 1/24$. According to this, a lower amount of hydrogen is available at the wire surface for diffusing towards inner points in the case of the lowest reduction ratio.

Therefore, it can be concluded that the effect of skin pass is also beneficial from the HE point of view for the reduction ratio $\lambda = 1/12$ since the hydrogen concentration is notably reduced in the prospective damage zone (up to a 30%) instead of the soft increment of hydrogen concentration at the wire surface. However, a better reduction of hydrogen concentration is obtained for a reduction ratio $\lambda = 1/24$. For this case, the hydrogen amount is lower at the wire surface (10%) and, also, it is lower (40%) throughout the prospective damage zone. Consequently, the hydrogen microstructural damage leading to final catastrophic failure [49–53] will be lower too, and the susceptibility of such a wire to the HE-related phenomena will be lower.

To go further in the analysis, the time evolution of the hydrogen accumulation is shown in Figure 11 for two positions of relevance, r/a = 0.48 and r/a = 0.90.

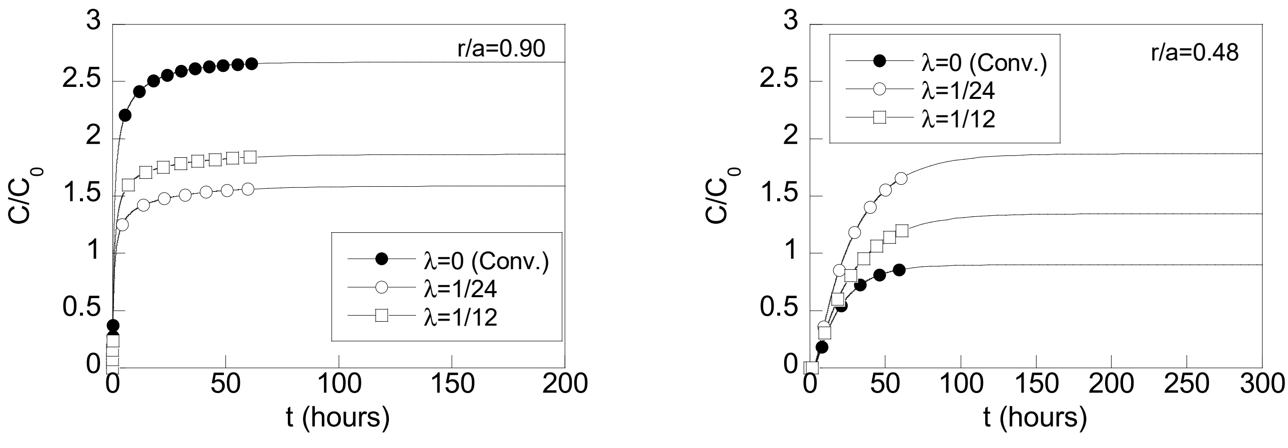

Figure 11. Time evolution of hydrogen concentration for wires drawn with optimal skin pass dies (blank symbols) and with conventional dies (filled circles) at: (**a**) prospective damage zone, r/a = 0.90 and (**b**) inner points, r/a = 0.48.

The time evolution of hydrogen concentration reveals how hydrogen is accumulated at certain points of interest. In this study, the main attention is focused on the prospective damage zone (5.0 mm < r < 5.4 mm) and the zone where the hydrogenation of wires drawn with modified dies were higher than the hydrogenation in conventional wires (2.0 mm < r < 4.0 mm). Thus, at the prospective damage zone (Figure 11a), the hydrogen amount obtained with modified dies is notably lower than the hydrogen concentration obtained in a conventional wire drawn as previously discussed. In addition, the slope of the curves shows that the hydrogen accumulation is about a 30% faster in conventional wires reaching a high amount of hydrogen sooner than wires drawn with modified dies including a skin pass zone. Thus, the beneficial effect of using skin pass dies is again revealed since the hydrogen accumulation is lower and also slower than the one appearing in wires using conventional dies.

In the case of inner points, r/a = 0.48 (Figure 11b), the trend of hydrogen accumulation is just the opposite. This way, the hydrogen accumulation is higher and faster for wires drawn with dies including a skin pass zone, being faster for low reduction ratios (16% for $\lambda = 1/12$ and 52% faster for $\lambda = 1/24$ regarding to a conventional wire). This way, these results reveal the beneficial effect of inner compressive stress obtained in conventional wires acting against hydrogen diffusion. It is worth highlighting that the slopes of the hydrogen accumulation curves are smoother than those observed at the prospective damage zone (Figure 11a), or, in other words, the hydrogen accumulation at the inner points is notably slower than the one at the wire surface surroundings. So, it can be concluded that at inner points, the hydrogen concentration reaches lower values than at the wire surface surroundings and, also hydrogen accumulation takes more time at that place than at the wire surface surroundings. Consequently, hydrogen damage is less probable to occur at inner points of the wire.

5. Conclusions

In this paper, the effects of the skin pass technique on the residual stress and strain in cold drawn pearlitic steel wires are analyzed to reveal the optimal conditions to be used in the design of dies for wire drawing of commercial prestressing steel wires. According to results, the following conclusions can be drawn:

- The introduction in the wire drawing technique of a soft diameter reduction after the main one generates a decrease of residual stress distributions (both axial and hydrostatic) at the wire surface and its vicinity. Such a decrease leads to a practical elimination at the inner points of the wire.
- The secondary reduction degree is a key factor in the modified drawing process. Thus, as the value of such a parameter decreases, the stress state at inner points is progressively reduced up to becoming almost null at the wire core, whereas an important reduction is achieved at the wire surface.
- In the *innovative* (*non-conventional*) drawing procedure proposed in the present paper, an increment of the equivalent plastic strains is produced (compared to those obtained in a conventional wire drawing) as a result of the reduction of the wire diameter undergone in the skin pass zone.
- The *innovative* (*non-conventional*) drawing procedure leading to the optimal stress state from the structural integrity point of view is associated with a secondary wire diameter reduction values within the range $\Delta d_2 \in$ (50 µm, 100 µm).
- Hydrogen accumulation in the prospective damage zone (near the wire surface) is lower in the wires drawn by means of the *innovative* (*non-conventional*) drawing procedure described in this paper, the lowest values achieved for the case of a reduction ratio 1/24 (*soft secondary wire diameter reduction* Δd_2 = 50 µm).
- Hydrogen accumulation is also slower for the case of reduction ratio 1/24 in the prospective damage zone. For this reason, this case could be considered as the optimal one from both mechanical (lower residual stresses) and hydrogen embrittlement (lower and slower hydrogen accumulation) points of view.
- The hydrogen amount at the inner points of the wire is increased by reducing the compressive residual stress at inner points. Anyway, the hydrogen amount at these zones does not exceed the maximum hydrogen amount placed at the wire surface surroundings where the prospective hydrogen damage will take place.

Author Contributions: J.T. and M.L. conceived the research; M.L. designed the analysis, performed the numerical calculations and analyzed the data, J.T. and M.L. wrote the paper. All authors have read and agreed to the published version of the manuscript.

Funding: The authors wish to acknowledge the financial support provided by the following Spanish Institutions: Ministry for Science and Technology (MCYT; Grant MAT2002-01831), Ministry for Education and Science (MEC; Grant BIA2005-08965), Ministry for Science and Innovation (MICINN; Grant BIA2008-06810), Ministry for Economy and Competitiveness (MINECO; Grant BIA2011-27870), Junta de Castilla y León (JCyL; Grants SA067A05, SA111A07 and SA039A08).

Institutional Review Board Statement: Not applicable.

Informed Consent Statement: Not applicable.

Data Availability Statement: Not applicable.

Conflicts of Interest: The authors declare no conflict of interest. With regard to the research funds, the different institutions providing financial support for the scientific research had no role in the design of the study; in the collection, analyses, or interpretation of data; in the writing of the present manuscript; and in the decision to publish the results.

References

1. Lynch, S.P. Failures of structures and components by environmentally assisted cracking. *Eng. Fail. Anal.* **1994**, *1*, 77–90. [CrossRef]
2. Mallick, A.; Das, S.; Mathur, J.; Bhattacharyya, T.; Dey, A. Internal reversible hydrogen embrittlement leads to engineering failure of cold drawn wire. *Case Studies Eng. Fail. Anal.* **2013**, *1*, 139–143. [CrossRef]
3. Nakamura, S.-I.; Suzumura, K. Hydrogen embrittlement and corrosion fatigue of corroded bridge wires. *J. Constr. Steel Res.* **2009**, *65*, 269–277. [CrossRef]
4. Vehovar, L.; Kuhar, V.; Vehovar, A. Hydrogen-assisted stress-corrosion of prestressing wires in a motorway viaduct. *Eng. Fail. Anal.* **1998**, *5*, 21–27. [CrossRef]
5. Perrin, M.; Gaillet, L.; Tessier, C.; Idrissi, H. Hydrogen embrittlement of prestressing cables. *Corros. Sci.* **2010**, *52*, 1915–1926. [CrossRef]
6. Katagiri, K.; Sato, T.; Kasaba, K.; Sasaki, S.; Tashiro, H. Effects of post-drawing treatments on the fatigue strength of eutectoid steel wires. *Fatigue Fract. Eng. Mater. Struct.* **1999**, *22*, 753–760. [CrossRef]
7. Kuboki, T.; Kawakami, I.; Neishi, M.; Kuroda, K.; Akiyama, M. A study on the influence of mechanical properties on the distribution of axial residual stress after cold drawing of metallic bars. *Mater. Sci. Res. Int.* **2001**, *7*, 41–46. [CrossRef]
8. Asakawa, M.; Sasaki, W.; Shishidi, S. Effect of die approach geometry and bearing length on residual stress after bar drawing. *Wire J. Int.* **2012**, *1*, 68–72.
9. Kuboki, T.; Akiyama, M.; Neishi, Y.; Kuroda, K. Effect of final drawing with light reduction on the leveling of residual stress distribution in cold bar drawing. *P. I. Mech. Eng. C-J. Mec.* **2000**, *214*, 1389–1399. [CrossRef]
10. Toribio, J.; Lorenzo, M.; Vergara, D.; Kharin, V. Influence of the die geometry on the hydrogen embrittlement susceptibility of cold drawn wires. *Eng. Fail. Anal.* **2014**, *36*, 215–225. [CrossRef]
11. Överstam, H. The influence of bearing geometry on the residual stress state in cold drawn wire by the FEM. *J. Mater. Process. Technol.* **2004**, *171*, 446–450. [CrossRef]
12. Rodríguez, M.; Weygand, S.M.; Riedel, H. Reduction of tensile residual stresses during the drawing process of tungsten wires. *Mater. Sci. Eng. A* **2010**, *527*, 3064–3072. [CrossRef]
13. Lin, H.-S.; Hsu, Y.-C.; Keh, C.-C. Inhomogeneous deformation and residual stress in skin-pass axisymmetric drawing. *J. Mater. Process. Technol.* **2008**, *201*, 128–132. [CrossRef]
14. Toribio, J.; Lorenzo, M.; Vergara, D. On the use of varying die angle for improving the resistance to hydrogen embrittlement of cold drawn prestressing steel wires. *Eng. Fail. Anal.* **2015**, *47*, 273–282. [CrossRef]
15. Luis, C.J.; León, J.; Luri, R. Comparison between finite element method and analytical methods for studying wire drawing processes. *J. Mater. Process. Technol.* **2005**, *164–165*, 1218–1225. [CrossRef]
16. Celentano, D.J.; Palacios, M.A.; Rojas, E.L.; Cruchaga, M.A.; Artigas, A.A.; Monsalve, A.E. Simulation and experimental validation of multiple-step wire drawing processes. *Finite Elem. Anal. Des.* **2009**, *45*, 163–180. [CrossRef]
17. Weygand, S.M.; Riedel, H.; Eberhard, B.; Wouters, G. Numerical simulation of the drawing process of tungsten wires. *Int. J. Refract. Hard Met.* **2006**, *24*, 338–342. [CrossRef]
18. McAllen, P.J.; Phelan, P. Numerical analysis of axisymmetric wire drawing by means of a coupled damage model. *J. Mater. Process. Technol.* **2007**, *183*, 210–218. [CrossRef]
19. Radionova, L.V.; Lisovskiy, R.A.; Svistun, A.S.; Gromov, D.V.; Erdakov, I.N. FEM simulation analysis of wire drawing process at different angles dies on straight-line drawing machines. In *Proceedings of the 8th International Conference on Industrial Engineering ICIE 2022*, 1st ed.; Radionov, A.A., Gasiyarov, V.R., Eds.; Springer: Cham, Switzerland, 2023; pp. 769–778. [CrossRef]

20. Santana Martinez, G.A.; Ferro Dos Santos, E.; Kyo Kabayama, L.; Siqueira Guidi, E.; De Azevedo Silva, F. Influences of different die bearing geometries on the wire-drawing process. *Metals* **2019**, *9*, 1089. [CrossRef]
21. Vega, G.; Haddi, A.; Imad, A. Investigation of process parameters effect on the copper-wire drawing. *Mater. Des.* **2009**, *30*, 3308–3312. [CrossRef]
22. Santana Martinez, G.A.; Qian, W.L.; Kyo Kabayama, L.; Prisco, U. Effect of process parameters in copper-wire drawing. *Metals* **2020**, *10*, 105. [CrossRef]
23. Tiernan, P.; Hillery, M.T. Dieless wire drawing—An experimental and numerical analysis. *J. Mater. Process. Technol.* **2004**, *155–156*, 1178–1183. [CrossRef]
24. Toribio, J.; Lorenzo, M. On the use of multi-step dies for improving the performance against hydrogen embrittlement of cold drawn prestressing steel wires. *Materials* **2022**, *15*, 9085. [CrossRef] [PubMed]
25. Panteghini, A.; Genna, F. Effects of the strain-hardening law in the numerical simulation of wire drawing processes. *Comp. Mater. Sci.* **2010**, *49*, 236–242. [CrossRef]
26. Dixit, U.S.; Dixit, P.M. An analysis of the steady-state wire drawing of strain-hardening materials. *J. Mater. Process. Technol.* **1995**, *47*, 201–229. [CrossRef]
27. Chevalier, L. Prediction of defects in metal forming: Application to wire drawing. *J. Mater. Process. Technol.* **1992**, *32*, 145–153. [CrossRef]
28. Tang, K.K.; Li, Z.X.; Wang, J. Numerical simulation of damage evolution in multi-pass wire drawing process and its applications. *Mater. Des.* **2011**, *32*, 3299–3311. [CrossRef]
29. Baek, H.M.; Jin, Y.G.; Hwang, S.K.; Im, Y.-T.; Son, I.-H.; Lee, D.-L. Numerical study on the evolution of surface defects in wire drawing. *J. Mater. Process. Technol.* **2012**, *212*, 776–785. [CrossRef]
30. Roh, Y.-H.; Cho, D.; Choi, H.-C.; Yang, Z.; Lee, Y. Process condition diagram predicting onset of microdefects and fracture in cold bar drawing. *Metals* **2021**, *11*, 479. [CrossRef]
31. Ma, A.; Cheng, J.; Wei, D.; Li, Q.; Fang, F.; Li, Z. Experiments and numerical analyses on splitting fracture of wire under multi-pass drawing. *Eng. Fail. Anal.* **2022**, *134*, 106035. [CrossRef]
32. Ocenásek, J.; Rodriguez Ripoll, M.; Weygand, S.M.; Riedel, H. Multi-grain finite element model for studying the wire drawing process. *Comp. Mater. Sci.* **2007**, *39*, 23–28. [CrossRef]
33. Zhu, Y.K.; Chen, Q.Y.; Wang, Q.; Yu, H.Y.; Li, R.; Hou, J.P.; Zhang, Z.J.; Zhang, G.P.; Zhang, Z.F. Effect of stress profile on microstructure evolution of cold-drawn commercially pure aluminum wire analyzed by finite element simulation. *J. Mater. Sci. Technol.* **2018**, *34*, 1214–1221. [CrossRef]
34. Kim, J.-C.; Cheong, S.-K.; Noguchi, H. Residual stress relaxation and low- and high-cycle fatigue behavior of shot-peened medium-carbon steel. *Int. J. Fatigue* **2013**, *56*, 114–122. [CrossRef]
35. Toribio, J.; Kharin, V.; Lorenzo, M.; Vergara, D. Role of drawing-induced residual stresses and strains in the hydrogen embrittlement susceptibility of prestressing steels. *Corros. Sci.* **2011**, *53*, 3346–3355. [CrossRef]
36. Toribio, J.; Lorenzo, M.; Vergara, D.; Kharin, V. Hydrogen degradation of cold drawn wires: A numerical analysis of drawing-induced residual stresses and strains. *Corrosion* **2011**, *67*, 5001–5009. [CrossRef]
37. Toribio, J.; Kharin, V. Evaluation of hydrogen assisted cracking: The meaning and significance of the fracture mechanics approach. *Nucl. Eng. Des.* **1998**, *182*, 149–163. [CrossRef]
38. Toribio, J.; Kharin, V. A hydrogen diffusion model for applications in fusion nuclear technology. *Fusion Eng. Des.* **2000**, *51–52*, 213–218. [CrossRef]
39. Toribio, J.; Kharin, V.; Vergara, D.; Lorenzo, M. Two-dimensional numerical modelling of hydrogen diffusion in metals assisted by both stress and strain. *Adv. Mater. Res.* **2010**, *138*, 117–126. [CrossRef]
40. Toribio, J.; Kharin, V. A generalised model of hydrogen diffusion in metals with multiple trap types. *Phil. Mag.* **2015**, *95*, 3429–3451. [CrossRef]
41. Toribio, J.; Kharin, V. Hydrogen transport to fracture sites in metals and alloys: Multiphysics modelling. *Procedia Struct. Integr.* **2017**, *5*, 1291–1298. [CrossRef]
42. Panasyuk, V.V.; Ivanyts'kyi, Y.-L.; Hembara, O.V.; Boiko, V.M. Influence of the stress-strain state on the distribution of hydrogen concentration in the process zone. *Mater. Sci.* **2014**, *50*, 315–323. [CrossRef]
43. Toribio, J.; Ayaso, F.J.; Gonzalez, B.; Matos, J.C.; Vergara, D.; Lorenzo, M. Tensile fracture behaviour of progressively-drawn pearlitic steels. *Metals* **2016**, *6*, 114. [CrossRef]
44. Toribio, J.; Ovejero, M. Microstructure evolution in a pearlitic steel subjected to progressive plastic deformation. *Mater. Sci. Eng. A* **1997**, *234–236*, 579–582. [CrossRef]
45. Toribio, J.; Ovejero, E. Effect of cumulative cold drawing on the pearlite interlamellar spacing in eutectoid steel. *Scr. Mater.* **1998**, *39*, 323–328. [CrossRef]
46. Zienkiewicz, O.C.; Taylor, R.L. *The Finite Element Method Vols. 1–2*; McGraw-Hill: London, UK, 1991.
47. Hirth, J.P. Effects of hydrogen on the properties of iron and steel. *Metall. Trans. A* **1980**, *11*, 861–890. [CrossRef]
48. Lillard, R.S.; Enos, D.G.; Scully, J.R. Calcium hydroxide as a promoter of hydrogen absorption in 99.5% Fe and a fully pearlitic 0.8% C steel during electrochemical reduction of water. *Corrosion* **2000**, *56*, 1119–1132. [CrossRef]
49. Toribio, J.; Lancha, A.M.; Elices, M. Characteristics of the new tearing topography surface. *Scr. Metall. Mater.* **1991**, *25*, 2239–2244. [CrossRef]

50. Toribio, J.; Lancha, A.M.; Elices, M. The tearing topography surface as the zone associated with hydrogen embrittlement processes in pearlitic steel. *Metall. Trans.* **1992**, *23A*, 1573–1584. [CrossRef]
51. Toribio, J. Fracture mechanics approach to hydrogen-assisted microdamage in eutectoid steel. *Metall. Mater. Trans.* **1997**, *28A*, 191–197. [CrossRef]
52. Toribio, J. Time-dependent triaxiality effects on hydrogen-assisted microdamage evolution in pearlitic steel. *ISIJ Int.* **2012**, *52*, 228–233. [CrossRef]
53. Toribio, J.; Elices, M. Influence of residual stresses on hydrogen embrittlement susceptibility of prestressing steels. *Int. J. Solids Struct.* **1991**, *28*, 791–803. [CrossRef]